IOSR Journal Of Applied Physics (IOSR-JAP)
e-ISSN: 2278-4861.Volume 16, Issue 3 Ser. 1 (May. – June. 2024), PP 32-40
www.Iosrjournals.Org

Electrical And Antibacterial Study of Hydrothermally Synthesized α-Manganese Sulphide Nanoparticles

Devarshi H. Vyas*[,1], Dr. Ketan D. Parikh*[,1], Vijay R. Dubey [1],
Ravirajsinh J. Jadav [1], Dr. Chaitanya K. Jha [2], Dr. Keyur D. Bhatt [3]
[1] *Department of Physics, Gujarat Arts and Science College, Ahmedabad, India. 380006*
[2]*Department of Microbiology, Gujarat Arts and Science College, Ahmedabad, India. 380006*
[3]*Department of Chemistry, Ganpat University, Kherava, Mehsana, Gujarat-384012*

Abstract:
α-MnS nanoparticles (NPs) were successfully synthesized at 180°C through a hydrothermal method. All the reflections in the PXRD pattern of α-MnS could be indexed as a cubic structure. Elemental mapping analyzed through EDAX showed the presence of Mn and S without any impurities. FESEM micrographs and HRTEM images were clearly identified that α-MnS NPs have spherical type morphology. SAED shows ring pattern, which clearly state that MnS NPs have polycrystalline type of nature. A direct band gap of α-MnS NPs was found to be 2.00 eV using UV-visible spectroscopy. Furthermore, complex impedance spectroscopy, complex modulus spectroscopy and dielectric study were performed on α-MnS NPs to identified their electrical nature with contribution of grain and grain boundary. α-MnS NPs were tested against various bacterial strains. Among them, α-MnS NPs showed the maximum antibacterial activity against E. coli.

Key Word*: α-MnS NPs, PXRD, SEM, EDAX, UV-Visible spectroscopy, antibacterial, dielectric study, complex modulus/impedance spectroscopy*

Graphical Abstract:

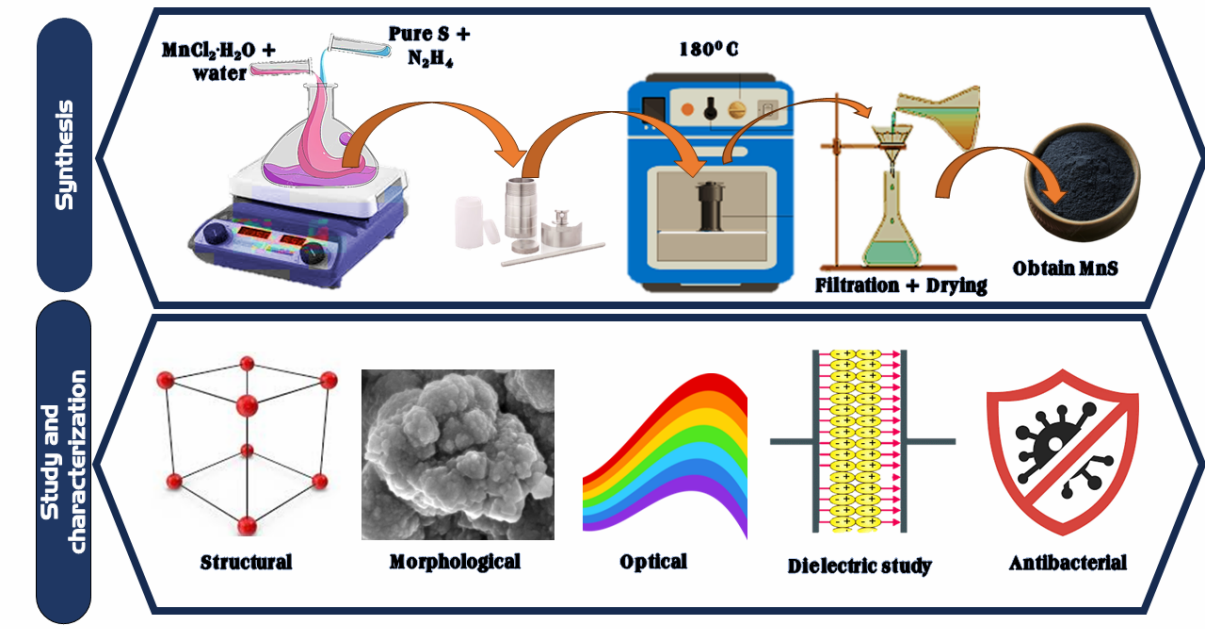

Date of Submission: 07-06-2024 Date of Acceptance: 17-06-2024

I. Introduction

In this modern age of scientific and technological progress, Transition Metal Sulfide (TMS) nanoparticles (NPs) have become a focal point for scientists and researchers due to their direct elemental sources in synthesis, offering a cost-effective solution.1-3 Over the past decade, diverse sectors such as electrical and optical industries have harnessed the significant benefits of TMS NPs, exploiting their varied

electronic, optical, and antimicrobial properties. With a surge of interest among researchers, investigations into various transition metal sulfides, such as CdS3,4, CuS5,6, CoS7,8, ZnS9,10, and MnS11-13, have been undertaken to analyze their synthesized nanoparticles. Among these, MnS nanoparticles hold particular promise due to their ability to be finely tuned in terms of size, shape, and surface characteristics, enhancing their utility across a wide array of applications.14-15 These nanoparticles manifest in distinct phases, including α-MnS, β-MnS, and γ-MnS, each exhibiting unique structural arrangements. Zhang et al.16 and Moloto17 have revealed that β and γ-MnS phases typically form under low-temperature conditions, transitioning to α-MnS at higher temperatures or pressures. Manipulation of the Mn to S ratio during the synthesis of MnS microparticles were investigated by T. Veeramanikandasamy et al.18, facilitates the formation of β-MnS and γ-MnS microparticles, characterized by specific molar ratios. MnS NPs emerge as a significant semiconductor material due to its intriguing characteristics, including a direct band gap, abundance in nature and non-toxicity. Additionally, Zein Heiba et al.19 was proposed that the absorption coefficient is enhanced while the static dielectric constant is decreased in all types of MnS samples. All these remarkable properties and diverse applications, authors are increasingly drawn to the synthesis of MnS NPs.

This paper introduces a hydrothermal method aimed at producing MnS NPs. The ensuing α-MnS crystallites underwent meticulous evaluation utilizing diverse characterization techniques, encompassing Rietveld analysis of powder x-ray diffraction (PXRD), scanning electron microscopy (SEM), energy-dispersive X-ray spectroscopy (EDAX), and X-ray photoelectron spectroscopy (XPS). Additionally, UV-visible spectral analysis was conducted to provide deeper insights the properties of the synthesized nanoparticles. This comprehensive characterization endeavor yielded invaluable insights into the structural, morphological, and chemical composition aspects of the freshly prepared α-MnS crystallites, thereby enriching our understanding of their potential applications. Furthermore, investigations into the electrical properties of α-MnS NPs were conducted through dielectric, complex impedance, and modulus studies, further advancing our knowledge of these materials.

II. Experimental:

Synthesis of MnS NPs:

The analytical grade manganese (II) chloride tetra-hydrate (MnCl2.4H2O), sulphur powder, methanol and hydrazine hydride (NH2NH2.H2O) were used as solvents and reagents for hydrothermal synthesis. In this process 0.2 mmol MnCl2.4H2O and pure sulphur powder were used as a 1:1 ratio in the solvents with vigorously stirred for 30 minutes. After the well stirring solution was transfer into teflon line autoclave and kept in hot-air oven at 180oC for 24 hours then cooled down at room temperature. The black color nanoparticles were found after filtered and washed. The chemical reactions can be expressed in two steps:

(1)

(2)

Characterization technique:

The powder X-ray diffractogram was carried out using Rigaku, model- miniflex-600 in the 2θ range of 20o to 80o with step size 0.02, using CuKα (1.5406Å). FULLPROF software package were utilized to performed Rietveld refinement of MnS NPs. UV-Vis. analysis was executed by Shimadzu UV 2600 spectrophotometer from the wavelength range of 200 nm to 800 nm at room temperature. The FESEM and EDAX were performed by using Carl Zeiss Model Supra 55 FESEM with a maximum resolution of 1 nm at 15 kV for morphology and elemental study respectively. The structure and morphology were recorded by High resolution transmission electron microscope (HRTEM) with JEOL JEM 2100 PLUS with 0.23 nm high resolution. The elemental analysis was performed by X-ray Photoelectron Spectroscopy (XPS) with Monochromatic X-ray Beam (15μm), X-ray beam induced secondary electron imaging and chemical state imaging, Large/Micro area and Angle dependent XPS. The dielectric study was studied by measuring using an Agilent-E4980A Precision LCR meter at room temperature from the range of 20 kHz to 2 MHz

Biological essay:

The Muller Hinton well diffusion method was used to study the antimicrobial screening of the synthesized MnS NPs by zone of inhibition method.6,20 The Gram (+ve) positive bacteria, Staphylococcus aureus (MTCC-96) and Streptococcus pyogenes (MTCC-443), Gram (-ve) negative bacteria Escherichia coli (MTCC-442) and Pseudomonas aeruginosa (MTCC-441) were used as model test strains. Well of 6 mm diameter was made on plates using gel puncture. Synthesized NPs and standard drugs were dispersed in acetone in the concentration of 50 μg/mL. Chloramphenicol and Ciprofloxacin, were used as standard drugs. Double distilled water was used as a control.

III. Results And Discussion:

Powder XRD:

The Powder X-ray diffraction patterns of α-MnS NPs was Rietveld refined using FULLPROF software. The observed, calculated and difference patterns of the compounds in the XRD profile are shown in Fig. 1 (a). Based on the refined parameters, the cubic structure was found with space group of *Fm-3m*, shown in Fig. 1 (b). The lattice parameters found to be a = 5.224 Å, α = 90° and unit cell volume was determined 142.56 $Å^3$. Fig. 1 (c) and (d) shows 3D and 2D electron density distributions in the unit cell structure of α-MnS.

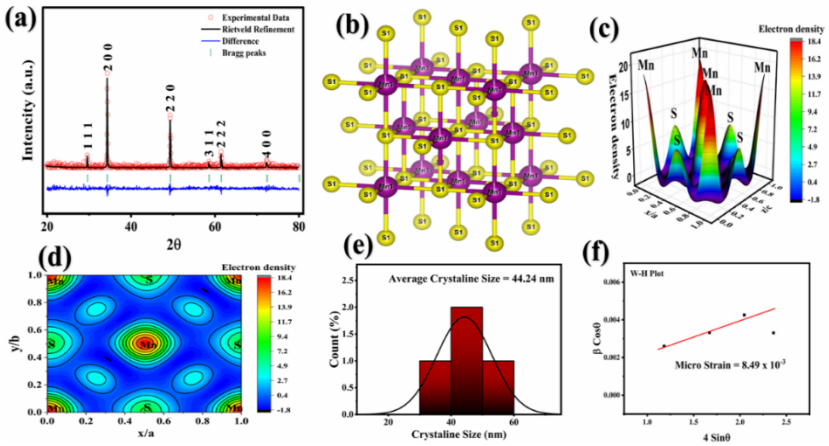

Fig. 1 (a) Rietveld refined XRD profile, (b) unit cell crystal structure, (c) 3D, (d) 2D electron density distributions in the unit cell structure, (e) Histogram of average crystallite size from Debye–Scherrer formula and (f) W–H plot of α-MnS NPs.

The average crystallite size was calculated using Scherrer formula and was found to be 44.9 nm, obtained from histogram of fig 1(e). Williamson-Hall (W–H) plot is shown in Fig. 1(f), from this the average crystallite size and the lattice strain were determined 77.76 nm and 8.49×10^{-3} respectively, which are in close agreement with that of crystallite size obtained using Scherrer method. Average dislocation density was calculated and found to be 5.11 $\times10^{14}$ m^{-2}. Average lattice constant was calculated to be 5.2163 Å from the d spacing of corresponding (h, k, l) parameters.

Elemental analysis:

The stoichiometric chemical composition of the synthesized α-MnS NPs was assessed using the EDAX technique. Fig. 2 (a) presents the obtained EDAX spectrum, depicting the weight and atomic percentage data showcased via pie charts. Additionally, Fig. 2 (b) illustrates the surface morphology of the synthesized sample, while Fig. 3(c) provides chemical mappings of the α-MnS NPs. Furthermore, Fig. 2 (d) and (e) exhibit the chemical distribution of Mn and S NPs, respectively. Notably, the EDAX spectrum revealed no presence of other elements, affirming the purity of the synthesized α-MnS NPs. This comprehensive analysis offers valuable insights into the chemical composition and morphology of the fabricated nanoparticles, ensuring their suitability for intended applications.

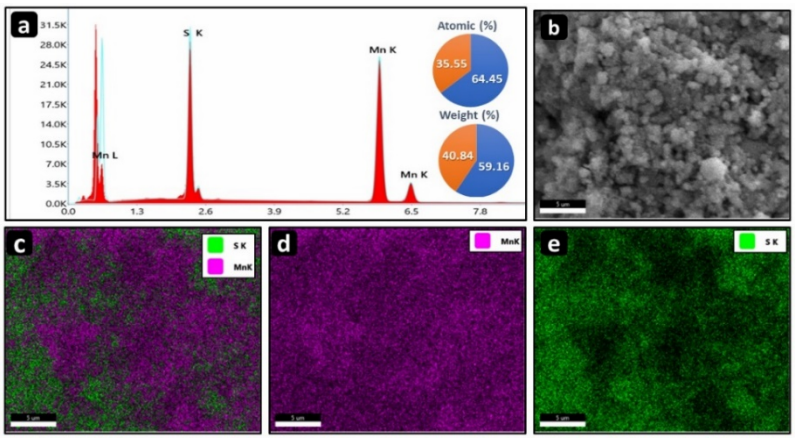

Fig 2 (a) EDAX Spectrum of α-MnS NPs (b) Surface morphology of α-MnS NPs (c) MnS NPs elemental mapping (d & e) distribution of chemical composition of Mn and S respectively

X-ray photoelectron spectroscopy (XPS) spectra were used to assess α-MnS NPs' chemical composition and states. Figure 3 (a) shows an XPS survey spectrum of α-MnS NPs, revealing the presence of *Mn*, *S*, *C*, and *O* elements. The high-resolution XPS spectrum of *Mn:2p* shown in Fig. 3 (b) demonstrates two prominent peaks at 649.9 eV and 638.2 eV, corresponding to $Mn{:}2p_{1/2}$ and $Mn{:}2p_{3/2}$ with a spin–orbit level energy spacing of 11.07 eV. These peak positions are associated to the Mn^{2+} ion of the α-MnS NPs[21]. For high-resolution spectrum of *S:2p* displayed in Fig. 3 (c), the two peaks at the binding energies of 162.2 eV and 154.1 eV ware attributed to *S:2p*, confirming the existence of S^{2-} ion in the α-MnS NPs, which correspond to $S{:}2p_{3/2}$ and $S{:}2p_{1/2}$ respectively with a spin–orbit level energy spacing of 8.01 eV.[22] The atomic weight percentages of $Mn{:}2p_{3/2}$ and $S{:}2p_{1/2}$ peaks were determined to be 54.8 and 45.2 respectively, indicating the formation of α-MnS NPs with excess Mn. The XPS analysis revealed that the chemical states of the α-MnS NPs contain Mn^{2+} and S^{2-}, which consistent the XRD and EDAX findings.

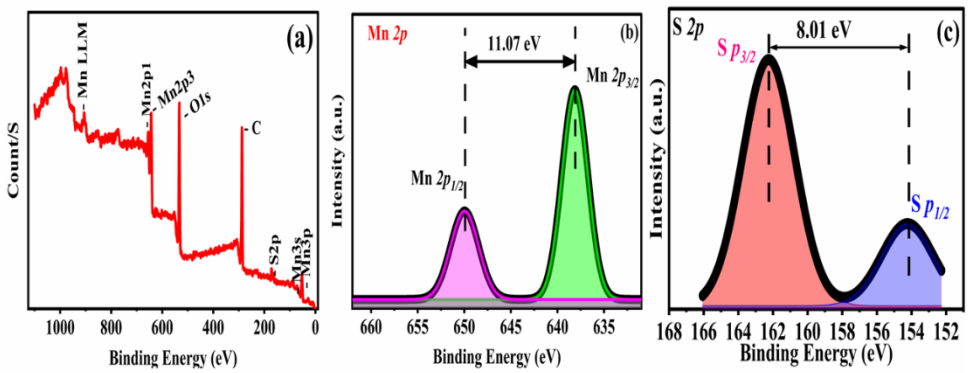

Fig 3 (a) XPS survey spectrum; high-resolution XPS spectra of MnS NPs (b) Mn 2p (c) S 2p

Morphological Study:

The morphology and microstructure of the resulting α-MnS NPs were investigated by using field emission scanning electron microscopy (FESEM) and high-resolution transmission electron microscopy (HRTEM). The FESEM images of α-MnS NPs shown in Fig. 4 (a-c) reveal several small spherical particles with collections ranging in size 80–90 nm with a comparatively narrow size distribution of α-MnS NPs formed in the same reaction condition. The morphologies of α-MnS NPs were also characterized by HRTEM and the results are shown in Fig. 4 (d-e), which also confirms spherical behavior of particles. Fig 4 (f) shows regular ring pattern in SAED image, which consistent with the PXRD results and suggests the polycrystalline nature of α-MnS NPs.

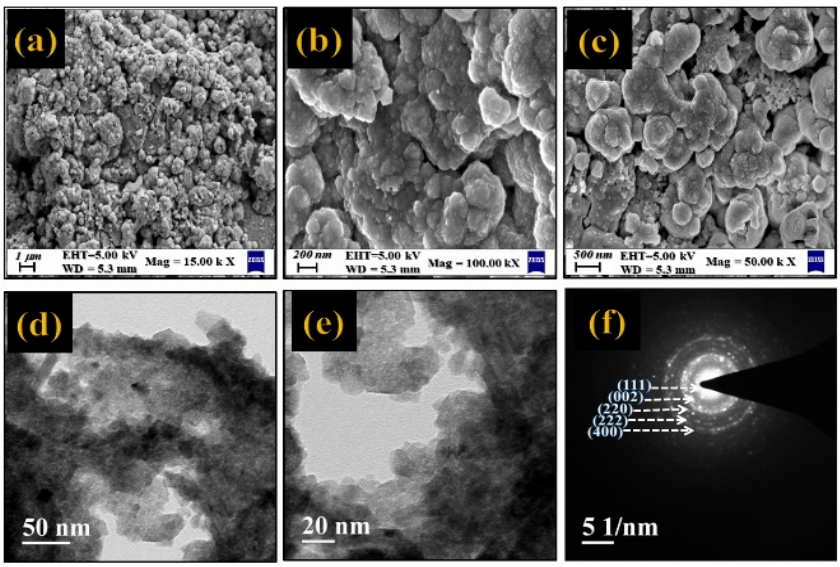

Fig. 4 (a-c) FESEM micrographs with different magnification (d-e) HRTEM images (f) SAED pattern of α-MnS NPs

Optical absorption Spectroscopy:

The optical absorption spectrum of α-MnS NPs was depicted in Fig. 5 (a), it is evident that the prepared α-MnS NPs exhibit absorption within the visible range, featuring a distinct absorption edge falling at wavelength of 350 nm.[22] This observation suggests that α-MnS NPs have been useful for UV absorption optical application. The plot depicted in Fig. 5 (b), showcasing $(\alpha h\nu)^2$ versus $h\nu$ for α-MnS NPs, reveals a direct optical bandgap. Notably, the value of bandgap differs from that reported for bulk material,[11,24] where the direct band gap tends to be higher. However, in the present case, for hydrothermally synthesized α-MnS nano-sized materials, this value found to be lesser than that bulk, around to be 2.00 eV.

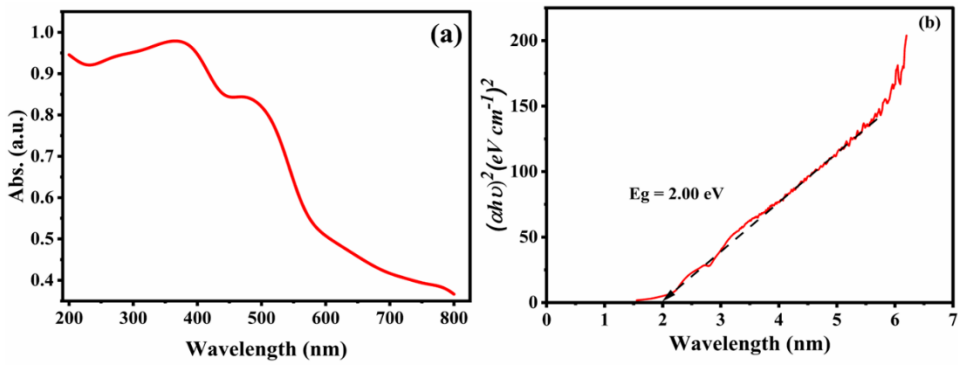

Fig. 5 (a) absorption and (b) Direct Bandgap of α-MnS NPs

Dielectric Study:

In Fig. 6 (a), the relationship between dielectric constant and logarithm of frequency is illustrated, revealing a trend where the dielectric constant is notably high at lower frequencies, gradually decreasing as frequency increases. This decline is attributed to the diminishing effect of space charge polarization, which establishes a potential barrier. However, in proximity to grain boundaries, there is an accumulation of charge, leading to heightened permittivity values. Interestingly, the dielectric dispersion observed is primarily influenced by the dominance of grain boundary effects rather than individual grains, a phenomenon elucidated by Koop's phenomenological theory. This behavior is attributed to Maxwell–Wagner type interfacial polarization.[25,26] In addition, total polarization within the material arises from multiple sources including ionic, electronic, dipolar, and space charge polarization, with electronic polarization having a relatively minor impact on the dielectric constant reduction.[4] Such polarization phenomena manifest due to the alignment of dipoles with the applied electric field, particularly prominent at lower frequencies, resulting in elevated dielectric constants. Conversely, at higher frequencies, the inability of dipoles to maintain alignment contributes to a decrease in the dielectric constant.

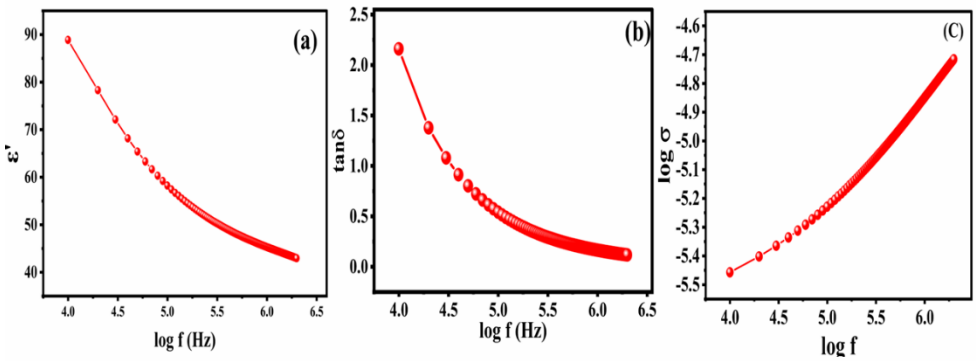

Fig. 6 (a) Dielectric constant vs *log f*, (b) Dielectric loss factor vs *log f* and (c) Johscher's plot of α-MnS NPs

The dielectric loss factor (*tanδ*) of a α-MnS NPs, determined by the ratio of energy dissipated to energy stored, plays a crucial role in understanding its behavior across different frequencies. In Fig. 6 (b), the relationship between dielectric loss and frequency at room temperature is depicted, showcasing a notable

decrease in *tanδ* with increasing frequency. This decline, particularly pronounced at higher frequencies, can be attributed to the suppression of domain wall motion. At the lower and intermediate frequencies, the dielectric loss exhibits higher values, likely due to various factors such as ion vibrations leading to ion jump and conduction loss, alongside ionic polarization effects. In the higher frequency range, ion vibrations become the predominant contributor to loss tangent, resulting in a decrease in dielectric loss.[7] Furthermore, the study highlights the adherence of α-MnS NPs to the Jonscher universal power law for a.c. conductivity is depicted in Fig. 6 (c), where the material exhibits frequency-independent conductivity behavior at lower frequencies, while increased with increasing frequency due to dispersion effects. The rise in conductivity leads to a corresponding increase in eddy currents, which subsequently enhances energy loss, represented by tan δ.[26]

Complex Impedance Spectroscopy:

Complex impedance spectroscopy (CIS) stands out as the most promising technique, not only for assessing but also for distinguishing the contributions of grain, grain boundary, and electrode effects to the polarization mechanism of the materials. Consequently, it provides insight into the charge carriers that affect the electrical properties within the respective regions i.e. grain and grain boundary of the prepared materials[7]. The complex impedance is determined by the equation: $Z^* = Z' + iZ''$, where Z' and Z'' are the real component and imaginary component of complex impedance respectively.

Figure 7 (a-b) illustrates the plots of the real component of impedance (Z') and the imaginary component of impedance (Z") against the logarithm of frequency. From the graphs, it is observed that both Z' and Z" decrease as the frequency increases. In Figure 7 (a), it can be noticed that at a higher frequency range, space charges are released, leading to the collapse of the curves. Figure 7 (b) shows a broad peak indicating an increase in frequency, with the intensity of this peak gradually diminishing. The presence of relaxation peaks within the broad peak suggests non-Debye behavior, characterized by a distribution of relaxation times. This implies that the material exhibits a range of relaxation dynamics rather than a single relaxation time, which is indicative of complex impedance behavior. [27,28]

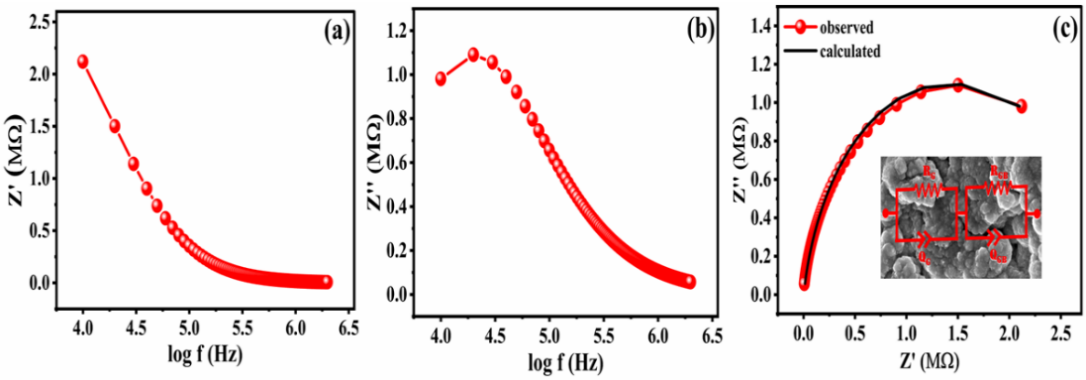

Fig. 7 (a) real part of impedance vs *log f*, (b) imaginary part of impedance vs *log f* and (c) Nyquist plot

The complex impedance plane (Nyquist plot), i.e. plot between Z' and Z'' is a useful approach to resolve the microstructural contributions to electrical transport based on the resistive and reactive response of the interface parts of the polycrystalline materials, depicted in Fig. 7 (c). Two parallel R-Q circuit presents inside fig 7 (c). The Constant phase element (Q) is introduced in the circuit corresponding to the grain boundary (g) properties due to non-ideal capacitive behavior, which may be due to the presence of more than one relaxation process with the same relaxation time (τ).[7] Impedance components were fitted with relaxation frequency (f_r), grain resistance (R_g), grain capacitance (C_g), grain relaxation time (τ_g), grain boundary resistance (R_{gb}), grain boundary capacitance (C_{gb}), and grain boundary relaxation time (τ_{gb}), which were determined as 19920.3 Hz, 192 KΩ, 2.59 x 10^{-11} F, 4.97 µS, 116 KΩ, 1.01x10^{-10} F, and 11.76 µS, respectively. Nyquist plot was also employed to characterize the modified electrode at various stages of platform construction.

Complex Modulus Spectroscopy:

Just like impedance spectroscopy, complex modulus spectroscopy also studies the electrical characteristics, like the relaxation time, polarization mechanism due to all the three effects which were bulk, grain boundary and the electrode and the involved conduction mechanism of the materials. However, the main characteristic of this spectroscopy is that it deals with the smallest capacitance, whereas the impedance spectroscopy deals with the largest resistance. It is formulated as: M* = M' + M'', where, M' and M'' are real part and imaginary part of the complex modulus.

Fig. 8 (a) describes the alteration of M' with frequency. It is noticed that, the value of M' rises with the increase in frequency and attains a constant value at a very high frequency. The reason for the above-mentioned behavior is that at lower frequency, the ions vibrate within the confinement of their potential energy well, whereas at higher frequency it remains insensitive to the electric field.[28] Fig. 8 (b) shows the graphical plot of frequency-dependent M'' curves. It is noticed that for the curves possess a relaxation peak. The reason behind this observation was the transition of mobility of charge carrier from a longer range to shorter range.[29] Fig. 8 (b) exhibits broad and asymmetric peaks indicating non-Debye type relaxation, i.e. the spreading of relaxation times.[30] The complex modulus formulation has been advantageous in terms of discrimination between electrode polarization and grain boundary conduction. At lower frequency the charge carriers are able to move within a long-range path under the effect of applied electric field, but due to lack of restoring force at this region the value of M' and M'' is quite smaller. The complex modulus spectra of M'' versus M' drawn semicircles in the complex plane as shown in Fig. 8 (c). The fig. 8 (c) clearly shows depressed semicircular arcs whose center does not lie on real axis.[7,30]

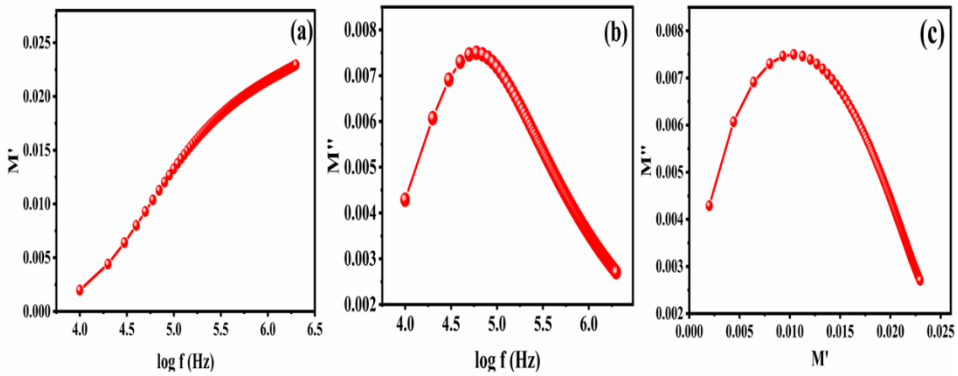

Fig:8 (a) Real part of modulus vs *logf*, (b) Imaginary part of modulus vs *logf* and (c) M'' vs M' plot

Antibacterial Study:

In the present study α-MnS NPs were experienced for antibacterial screening by inhibit the growth of Staphylococcus aureus and Streptococcus pyogenes for gram-positive and Escherichia coli and Pseudomonas aeruginosa for gram-negative bacteria. The results of antibacterial activity revealed that of synthesized α-MnS NPs indicated weak to good activities against all tested microorganisms as compared to standard drugs. It was observed in fig 9 that α-MnS NPs exhibited good activity against both *E. coli*, while displayed weak activity against other tested microbes with comparison to chosen standard drugs like Ciprofloxacin and Chloramphenicol.

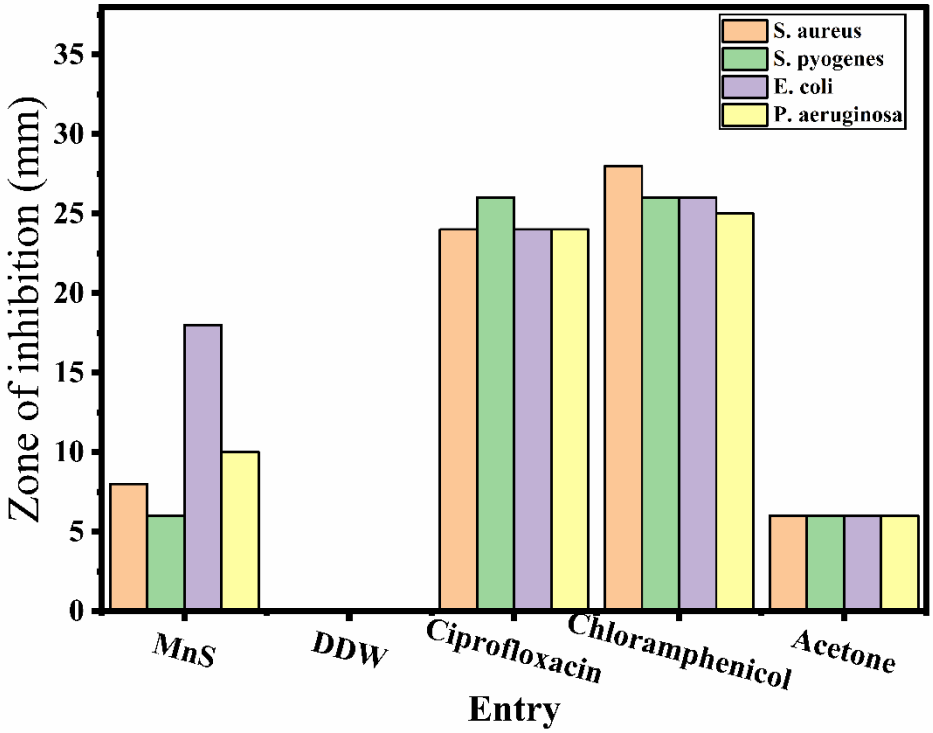

Fig: 9 antibacterial strains against α-MnS NPs, solvents and standard drugs

IV. Conclusions:

α-MnS NPs were synthesized by hydrothermal technique. The Rietveld refinement XRD analysis were showed the cubic structure of α-MnS NPs. The crystallite size was determined using Scherrer's equation and Williamson-Hall plot. In addition, residual compressive strain, dislocation density and crystallinity were evaluated. Morphological study shows α-MnS NPs have in spherical shape NPs. The elemental and chemical states were analyzed using EDAX and XPS spectra. The optical energy bandgap determined from the optical absorbance spectrum and found to be 2.00 eV. Dielectric constant and dielectric loss factor were observed maximum at lower frequencies due to space charge polarization and rapidly falls with increase in frequency. α-MnS NPs has frequency independent nature at lower frequency region, while frequency increases the conductivity increase. The impedance and modulus plots confirmed the dispersive nature and contribution of grain and grain boundary in present system. The asymmetric nature of imaginary part of impedance and modulus indicated non-Debye type relaxation. Antibacterial activity revealed that of synthesized α-MnS NPs indicated weak to good activities against all tested microorganisms as compared to standard drugs. It was observed that α-MnS NPs exhibited good activity against both E. coli, while displayed weak activity against S. Aureus S. Pyogenes and P. aeruginosa with comparison to chosen standard drugs.

References

[1] Mulla, R., Rabinal, M.K. Large-Scale Synthesis of Copper Sulfide By Using Elemental Sources Via Simple Chemical Route. Ultrasonics Sonochemistry 39, (2017), 528–533. Https://Doi.Org/10.1016/J.Ultsonch.2017.05.027.

[2] Ghanbari, B., Jamali-Sheini, F., Yousefi, R. Microwave-Assisted Solvothermal Synthesis And Optoelectronic Properties Of Γ-Mns Nanoparticles. Journal Of Materials Science: Materials In Electronics 29, (2018) 10976–10985. Https://Doi.Org/10.1007/S10854-018-9179-9.

[3] Jing, Z., Tan, L., Li, F., Wang, J., Fu, Y., Li, Q. Photocatalytic And Antibacterial Activities Of Cds Nanoparticles Prepared By Solvothermal Method. Indian J Chem. (2013).

[4] Suresh, S., 2014. Studies On The Dielectric Properties Of Cds Nanoparticles. Appl Nanosci 4, (2014) 325–329. Https://Doi.Org/10.1007/S13204-013-0209-X

[5] Tank, Nirali.S., Parikh, K.D., Joshi, M.J. Synthesis And Characterization Of Copper Sulphide (Cus) Nano Particles. Presented At The Functional Oxides And Nanomaterials: Proceedings Of The International Conference On Functional Oxides And Nanomaterials, Gujarat, India, (2017) P. 040018. Https://Doi.Org/10.1063/1.4982102.

[6] Bekhit, M., Abo El Naga, A.O., El Saied, M., Abdel Maksoud, M.I.A. Radiation-Induced Synthesis Of Copper Sulfide Nanotubes With Improved Catalytic And Antibacterial Activities. Environ Sci Pollut Res 28, (2021), 44467–44478. Https://Doi.Org/10.1007/S11356-021-13482-9.

[7] Joshi, J.H., Kanchan, D.K., Joshi, M.J., Jethva, H.O., Parikh, K.D. Dielectric Relaxation, Complex Impedance And Modulus Spectroscopic Studies Of Mix Phase Rod Like Cobalt Sulfide Nanoparticles. Materials Research Bulletin 93, (2017), 63–73. Https://Doi.Org/10.1016/J.Materresbull.2017.04.013.

[8] Pandey, A., Yadav, P., Biswal, R., Fahad, A., Khan, B., Kumar, P., Singh, M.K., 2024. Structural, Morphological And Electrical Properties Of Hydrothermally Synthesized Cobalt Disulfide (Cos_2) Nanoparticles. Ferroelectrics 618, (2024) 451–463. Https://Doi.Org/10.1080/00150193.2023.2273722.
[9] Wadhwani, M., Jain, S. Synthesis And Antimicrobial Activity Of Zinc Sulphide Nanoparticles 4. Issn 2277 (2015).
[10] Vijai Anand, K., Vinitha, G., Karl Chinnu, M., Mohan, R., Jayavel, R. Enhanced Third-Order Nonlinear Optical Properties Of High Purity Zns Nanoparticles. J. Nonlinear Optic. Phys. Mat. 24, (2015) 1550016. Https://Doi.Org/10.1142/S0218863515500162.
[11] Ibrahim, S.G. Physical Properties Of Chemically Spray Deposited Nanocrystalline Manganese Sulfide (Mns) Thin Films. J Mater Sci: Mater Electron 32, (2021)543–550. Https://Doi.Org/10.1007/S10854-020-04837-Y.
[12] Bera, A., Hasan, Md.N., Pan, N., Ghosh, R., Alsantali, R.A., Altass, H.M., Obaid, R.J., Ahmed, S.A., Pal, S.K. Implementation Of Surface Functionalization Of Mns Nanoparticles For Achieving Novel Optical Properties And Improving Therapeutic Potential. Rsc Adv. 12, (2022), 20728–20734. Https://Doi.Org/10.1039/D2ra01087a.
[13] Ali, I.M., Ibrahim, I.M., Ahmed, E.F., Abbas, Q.A. Structural And Characteristics Of Manganese Doped Zinc Sulfide Nanoparticles And Its Antibacterial Effect Against Gram-Positive And Gram-Negative Bacteria. Ojbiphy 06, (2016) 1–9. Https://Doi.Org/10.4236/Ojbiphy.2016.61001.
[14] Peng, L., Shen, S., Zhang, Y., Xu, H., Wang, Q. Controllable Synthesis Of Mns Nanocrystals From A Single-Source Precursor. Journal Of Colloid And Interface Science 377, (2012) 13–17. Https://Doi.Org/10.1016/J.Jcis.2012.03.052.
[15] M. Ferretti, A., Mondini, S., Ponti, A. Manganese Sulfide (Mns) Nanocrystals: Synthesis, Properties, And Applications, In: Muzibur Rahman, M., Mohamed Asiri, A. (Eds.), Advances In Colloid Science. (2016) Intechopen. Https://Doi.Org/10.5772/65092.
[16] Zhang, Y., Wang, H., Wang, B., Yan, H., Yoshimura, M. Low-Temperature Hydrothermal Synthesis Of Pure Metastable Γ-Manganese Sulfide (Γ-Mns) Crystallites. Journal Of Crystal Growth. (2002).
[17] Moloto, N., Moloto, M.J., Kalenga, M., Govindraju, S., Airo, M. Synthesis And Characterization Of Mns And Mnse Nanoparticles: Morphology, Optical And Magnetic Properties. Optical Materials 36, (2013) 31–35. Https://Doi.Org/10.1016/J.Optmat.2013.06.023.
[18] Heiba, Z.K., Mohamed, M.B., Badawi, A., Farag, N.M., 2021. Effect Of Sulfur Deficiency On The Structural, Optical And Electronic Properties Of Mns Nanostructures. Chemical Physics Letters 779, (2021) 138877. Https://Doi.Org/10.1016/J.Cplett.2021.138877.
[19] Geetha, G., Murugasen, P., Sagadevan, S. Synthesis And Characterization Of Manganese Sulphide Thin Films By Chemical Bath Deposition Method. Acta Phys. Pol. A 132, (2017) 1221–1226. Https://Doi.Org/10.12693/Aphyspola.132.1221.
[20] Trivedi, H.D., Patel, B.Y., Patel, P.K., Sagar, S.R. Synthesis, Molecular Modeling, Admet And Fastness Studies Of Some Quinoline Encompassing Pyrimidine Azo Dye Derivatives As Potent Antimicrobial Agents. Chemical Data Collections 41, (2022) 100923. Https://Doi.Org/10.1016/J.Cdc.2022.100923.
[21] Tailor, J.P., Khimani, A.J., Chaki, S.H., Deshpande, M.P. Thermal Decomposition Study Of Manganese Sulfide (Mns) Nanoparticles. Presented At The 2nd International Conference On Condensed Matter And Applied Physics (Icc 2017), Bikaner, India, (2018) P. 030197. Https://Doi.Org/10.1063/1.5032532
[22] Hussain, S., Akbar, K., Vikraman, D., Liu, H., Chun, S.-H., Jung, J. Ws_2/$Cose_2$ Heterostructure: A Designed Structure As Catalysts For Enhanced Hydrogen Evolution Performance. Journal Of Industrial And Engineering Chemistry 65, (2018) 167–174. Https://Doi.Org/10.1016/J.Jiec.2018.04.025.
[23] Chaki, S.H., Chauhan, S.M., Tailor, J.P., Deshpande, M.P., 2017. Synthesis Of Manganese Sulfide (Mns) Thin Films By Chemical Bath Deposition And Their Characterization. Journal Of Materials Research And Technology 6, (2017) 123–128. Https://Doi.Org/10.1016/J.Jmrt.2016.05.003.
[24] Lokhande, C.D., Ennaoui, A., Patil, P.S., Giersig, M., Muller, M., Diesner, K., Tributsch, H. Process And Characterisation Of Chemical Bath Deposited Manganese Sulphide (Mns) Thin Films. Thin Solid Films 330, (1998) 70–75. Https://Doi.Org/10.1016/S0040-6090(98)00500-8.
[25] Javed, M., Khan, A.A., Akbar, N., Kazmi, J., Dar, A., Mohamed, M.A. Low-Temperature Dielectric Relaxation Mechanism And Correlated Barrier Hopping Transport In Neodymium Perovskite Chromite. Materials Research Bulletin 165, (2023) 112303. Https://Doi.Org/10.1016/J.Materresbull.2023.112303.
[26] Aparna, P.U., Divya, N.K., Pradyumnan, P.P., 2016. Structural And Dielectric Studies Of Gd Doped Zno Nanocrystals At Room Temperature. Msce 04, 79–88. Https://Doi.Org/10.4236/Msce.2016.42009
[27] Ahmad, F., Maqsood, A. Structural, Electric Modulus And Complex Impedance Analysis Of Zno At Low Temperatures. Materials Science And Engineering: B 273, (2021) 115431. Https://Doi.Org/10.1016/J.Mseb.2021.115431.
[28] Gupta, P., Meher, L.K., Choudhary, R.N.P. Structural, Dielectric, Impedance And Modulus Spectroscopy Of $Bila_2tivo_9$ Ceramic. Applied Physics A 126, (2020) 187. Https://Doi.Org/10.1007/S00339-020-3341-Y.
[29] Parida, K., Dehury, S.K., Choudhary, R.N.P. Structural, Electrical And Magneto-Electric Characteristics Of $Bimgfeceo_6$ Ceramics. Physics Letters A 380, (2016) 4083–4091. Https://Doi.Org/10.1016/J.Physleta.2016.10.022.
[30] Naik, J., Bhajantri, R.F., Rathod, S.G., Sheela, T., Ravindrachary, V. Synthesis And Characterization Of Multifunctional $Znbr_2$ /Pva Polymer Dielectrics. J. Adv. Dielect. 06, (2016) 1650028. Https://Doi.Org/10.1142/S2010135x16500284.

Funding
This work was funded by SHODH Scholarship (202001670085), Gujarat Government, India.

Acknowledgements

The authors express their gratitude to the Department of Physics at Gujarat Arts & Science College, Ahmedabad. The authors are appreciative of the support provided by Dr. Bharat Katariya and Mr. Mayurshinh Vala from the Department of Nano Science and Advanced Materials at Saurashtra University, Rajkot, for their assistance in the Dielectric study. The authors are also thankful for the support of Prof. Dr. Mihir J. Joshi, Dr. Nikesh Shah, Dr. Piyush Solanki, and Dr. H.O. Jethava from the Department of Physics at Saurashtra University, Rajkot, in their research. Additionally, the authors are grateful to the Department of Physics at Ganpat University, Kherava, Mehsana, for providing research facilities.